

Electromagnetic Torques, Precession and Evolution of Magnetic Inclination of Pulsars

J. J. Zanazzi^{1*}, and Dong Lai¹

¹*Center for Space Research, Department of Astronomy, Cornell University, Ithaca, New York 14853*

29 August 2018

ABSTRACT

We present analytic calculations of the electromagnetic torques acting on a magnetic neutron star rotating in vacuum, including near-zone torques associated with the inertia of dipole and quadrupole magnetic fields. We incorporate these torques into the rotational dynamics of a rigid-body neutron star, and show that the effects of the inertial torque can be understood as a modification of the moment of inertia tensor of the star. We apply our rotational dynamics equation to the Crab pulsar, including intrinsic distortions of the star and various electromagnetic torques, to investigate the possibility that the counter-alignment of the magnetic inclination angle, as suggested by recent observations, could be explained by pulsar precession. We find that if the effective principal axis of the pulsar is nearly aligned with either the magnetic dipole axis or the rotation axis, then precession may account for the observed counter-alignment over decade timescales. Over the spindown timescale of the pulsar, the magnetic inclination angle always decreases.

Key words: stars: neutron - stars: rotation - stars: magnetic fields

1 INTRODUCTION

The structure and evolution of magnetic fields is one of the key ingredients to understanding various observational manifestations of radio pulsars and other types of neutron stars (NSs) (e.g., Harding & Lai 2006; Kaspi 2010; Reisenegger 2013). For radio pulsars, the magnetic inclination angle α , defined as the angle between the pulsar’s magnetic dipole axis and rotation axis, strongly affects the pulse and polarization profiles in radio and high energy emissions (e.g., Rookyard et al. 2015). By analyzing polarization data for a large number of pulsars, Tauris & Manchester (1998) found that, statistically, pulsars with large characteristic ages tend to have small magnetic inclination angles, suggesting that the magnetic axis align with the spin axis on a timescale of order 10^7 years (see Weltevrede & Johnston 2008 and Young et al. 2010, who found somewhat different alignment timescales). On the other hand, general pulsar population studies have revealed no evidence for significant torque decay (due to magnetic field decay or alignment) over the pulsar lifetime ($\sim 10^8$ years) (e.g., Faucher-Giguère & Kaspi 2006; Gullón et al. 2014).

Recently, Lyne et al. (2013) found that the radio pulse profile of the Crab pulsar has shown a steady increase in the separation of the main pulse and interpulse components at 0.6° per century over 22 years (see also Lyne et al.

2015). The increase in pulse separation was interpreted as an increase in the magnetic inclination angle α . (see Watters et al. 2009). This interpretation is also consistent with departure of the braking index $n = (\omega\dot{\omega})/\dot{\omega}^2$ from 3 for the Crab pulsar (where ω is the angular rotation frequency). Using the braking torque due to a rotating magnetic dipole in vacuum, $\dot{\omega} \propto -\omega^3 \sin^2 \alpha$, and assuming a constant magnetic dipole moment, the braking index is given by

$$n = 3 + 2 \frac{\omega}{\dot{\omega}} \frac{\dot{\alpha}}{\tan \alpha}. \quad (1)$$

With the observed $\dot{\alpha} = 0.6^\circ/\text{century}$ and $\omega/\dot{\omega} = -24.9\text{century}$, and the estimate $\alpha \approx 45^\circ$ (Harding et al. 2008), we find $n \approx 2.48$, in agreement with the observed value of $n \simeq 2.50$ (Lyne et al. 2013).

The increase in the magnetic inclination angle cannot be explained by the simplest dynamical model of neutron stars (NSs). If one models a NS as a spherical body endowed with a frozen-in dipole magnetic field in vacuum, one expects only a decrease in the magnetic inclination angle (Davis & Goldstein 1970). Including the electro-dynamical effects of the magnetosphere leads to pulsar spindown even when the NS has an aligned dipole field ($\alpha = 0$) (Spitkovsky 2006; Kalapotharakos & Contopoulos 2009; Kalapotharakos et al. 2012; Tchekhovskoy et al. 2013), but still predicts magnetic alignment with the rotation axis (Philippov et al. 2014). While these results may be consistent with pulsar population statistics (Tauris & Manchester

* Email: jjz54@cornell.edu

1998), the short-term (~ 10 years) increase of α observed in the Crab pulsar is unaccounted for.

A possible physical mechanism for magnetic counter-alignment (increase of α) is pulsar precession, a topic of interest for nearly half a century. Early models of free precession modeled the NS as a rigid body undergoing a torque due to angular momentum loss from dipole radiation (Davis & Goldstein 1970; Goldreich 1970). Then came the inclusion of the pinned superfluid in the NS crust, which was shown to severely alter the rotational dynamics of NSs (Shaham 1977; Alpar et al. 1984; Alpar & Oegelman 1987; Casini & Montemayor 1998; Sedrakian et al. 1999; Link & Cutler 2002). The effects of super-fluidity “destroyed” precession, speeding it up to a rate undetectable by observations. But tentative observational evidence suggested that some pulsars precessed with periods comparable to those predicted by free precession (Suto & Iso 1985; Truemper et al. 1986; Lyne et al. 1988; Weisberg et al. 2010; Makishima et al. 2014). This led many to still model the precession of NSs as free, rather than forced (Link & Epstein 1997; Melatos 1997, 1999, 2000; Jones & Andersson 2001; Link & Epstein 2001; Wasserman 2003), and to infer interior physics which would lead to weak coupling between the crust and the core. Overall, despite the uncertainties, free precession remains a possible model for understanding the rotational behavior of NSs (Jones 2012).

In this paper, we treat the NS as a non-spherical rigid body acted upon by electromagnetic (EM) torques. Section 2 presents our calculation of the EM torques, including both “inertial torques” associated with the inertia of the near-zone EM field, and dipole radiative torque. In section 3, we solve the equations of motion for the NS rotation analytically, reproducing results which before now were only studied numerically (Melatos 1999, 2000). We show that the main effects of the inertial torque may be understood by modifying the moment of inertia tensor of the NS. In section 4, we discuss applications to pulsars, and in particular to the observed magnetic inclination evolution of the Crab pulsar. In section 5, we summarize our findings, and discuss various uncertainties and possible future works.

2 EM TORQUES ON ROTATING NS IN VACUUM

In this section, we calculate the EM torques on a rotating, magnetized sphere in vacuum. We consider both dipole and quadrupole magnetic field topologies. It is well known that a rotating magnetic NS must be surrounded by a magnetosphere with current and charge distributions (Goldreich & Julian 1969). This magnetosphere modifies the magnetic braking torque significantly (Spitkovsky 2006; Kalapotharakos & Contopoulos 2009; Philippov et al. 2014). However, the torque associated with the near-zone magnetic field inertia has not been calculated for magnetosphere models. We will show this inertial torque can significantly affect the precession dynamics of the NS.

2.1 Dipole Field

A spherical body with endowed with a dipole field rotating in vacuum has two torques acting on it. The first arises from

the fact that a misaligned spinning dipole emits EM radiation, carrying away angular momentum. We denote this torque as Γ_{rad} . The second torque arises from the inertia of the dipole magnetic field (Davis & Goldstein 1970), which we will denote by Γ_P . Our calculation yields the expressions (see Appendix A)

$$\Gamma_{\text{rad}} = \frac{2\omega^2}{3c^3}(\boldsymbol{\omega} \times \mathbf{p}) \times \mathbf{p}, \quad (2)$$

$$\Gamma_P = \frac{3}{5Rc^2}(\mathbf{p} \cdot \boldsymbol{\omega})(\mathbf{p} \times \boldsymbol{\omega}), \quad (3)$$

where $\boldsymbol{\omega}$ is the rotation rate vector, \mathbf{p} is the dipole moment, $p = |\mathbf{p}| = B_P R^3/2$, with B_P the magnitude of the fields at the magnetic poles, and R is the radius of the NS.

Note that the numerical coefficient $3/5$ in front of the expression for Γ_P agrees with Melatos (1997), but disagrees with Davis & Goldstein (1970), Goldreich (1970), Good & Ng (1985), and Beskin et al. (2013), all of whom quoted slightly different values. Our equation (3) is obtained by assuming a uniform interior field \mathbf{B}_P which rotates rigidly around the spin axis, and an electric field given by $\mathbf{E} = -(\mathbf{v}/c) \times \mathbf{B}_P$. Although this interior EM field was assumed, equation (3) only depends on the exterior EM field on the surface of the NS [see Eq. (71) in Appendix].

The difference between our value and that given by Good & Ng (1985) and Beskin et al. (2013) may be attributed to the method used to calculate the torque. These authors obtained the torque directly through the volume integral

$$\boldsymbol{\Gamma} = \int \mathbf{r} \times \left(\rho_e \mathbf{E} + \frac{1}{c} \mathbf{j}_e \times \mathbf{B} \right) dV, \quad (4)$$

and adopted specific assumptions on the charge density ρ_e and the current density \mathbf{j}_e inside the NS. Beskin et al. (2013) also included the effects of the EM field’s inertia. The difference from the value of Davis & Goldstein (1970) cannot be attributed to such a difference, as the authors appeared to have used the same method to calculate the torque. Beskin & Zheltoukhov (2014) also obtained the coefficient $3/5$ using the same approach as ours, although they questioned its validity of the method, suggesting that the final answer depends on the internal current distribution inside the rotating NS. Indeed, the angular momentum carried by the EM field is

$$\mathbf{L}_{\text{EM}} = \frac{1}{4\pi c} \int \mathbf{r} \times (\mathbf{E} \times \mathbf{B}) dV. \quad (5)$$

The rate of change of \mathbf{L}_{EM} due to stellar rotation is of order

$$\Omega |\mathbf{L}_{\text{EM}}| \sim \frac{B_P^2 R^5 \Omega^2}{c^2} \sim \frac{p^2 \Omega^2}{Rc^2}, \quad (6)$$

the same order as equation (3). Thus, including \mathbf{L}_{EM} into the angular momentum equation amounts to a modification of the inertial torque expression (3) by a factor of order unity [see Eq. (21) of section 3.1]. In the remainder of this paper, we adopt equation (3) as the inertial torque and do not include \mathbf{L}_{EM} into the dynamical equation for the NS. Since the precise value of B_P is uncertain by at least a factor of two, and more importantly, since the NS suffers a much larger deformation than that associated with the field inertia (see section 4.1), a correction to equation (3) by a factor of

order unity does not affect the main results of our paper (see sections 3-4).

For convenience, we define the dimensionless parameter ϵ_P as

$$\epsilon_P \equiv \frac{3}{20} \frac{B_p^2 R^5}{I c^2}, \quad (7)$$

where I is the moment of inertia of NS. With this definition, Γ_P becomes

$$\Gamma_P = I \epsilon_P (\hat{\mathbf{p}} \cdot \boldsymbol{\omega}) (\hat{\mathbf{p}} \times \boldsymbol{\omega}), \quad (8)$$

where $\hat{\mathbf{p}} = \mathbf{p}/p$ is the unit vector along the dipole axis. Thus, a change of the coefficient in equation (3) amounts to a modification of the value of ϵ_P by a factor of order unity.

2.2 Quadrupole Field

We have also calculated the inertial torque for NSs with an arbitrary magnetic quadrupole moment \mathbf{Q} , where \mathbf{Q} is a symmetric trace-free tensor with eigenvectors $\hat{\mathbf{q}}_1$, $\hat{\mathbf{q}}_2$, and $\hat{\mathbf{q}}_3$, and eigenvalues Q_1 , Q_2 , and Q_3 (see Appendix). Before we state the result, we will explain our field decomposition. Because \mathbf{Q} is trace-free ($\sum_i Q_i = 0$), this quadrupole moment may be expressed as the sum of two linearly independent tensors: \mathbf{Q}_{\parallel} and \mathbf{Q}_{δ} . These two independent trace-free quadrupole tensors have components in the $\{\hat{\mathbf{q}}_i\}$ basis given by

$$\mathbf{Q}_{\parallel} = \begin{pmatrix} -Q_{\parallel}/2 & 0 & 0 \\ 0 & -Q_{\parallel}/2 & 0 \\ 0 & 0 & Q_{\parallel} \end{pmatrix}, \quad (9)$$

$$\mathbf{Q}_{\delta} = \begin{pmatrix} Q_{\delta} & 0 & 0 \\ 0 & -Q_{\delta} & 0 \\ 0 & 0 & 0 \end{pmatrix}, \quad (10)$$

where $Q_{\parallel} = Q_3$ and $Q_{\delta} = (Q_1 - Q_2)/2$. On the surface of the star $\mathbf{r} = R\hat{\mathbf{r}}$, the radial components of the magnetic fields are

$$\hat{\mathbf{r}} \cdot \mathbf{B}_{\parallel}(R\hat{\mathbf{r}}) = B_{\parallel} P_2(\hat{\mathbf{r}} \cdot \hat{\mathbf{q}}_3), \quad (11)$$

$$\hat{\mathbf{r}} \cdot \mathbf{B}_{\delta}(R\hat{\mathbf{r}}) = \frac{2B_{\delta}}{3} [P_2(\hat{\mathbf{r}} \cdot \hat{\mathbf{q}}_2) - P_2(\hat{\mathbf{r}} \cdot \hat{\mathbf{q}}_1)], \quad (12)$$

where $B_{\parallel} = -2Q_{\parallel}/R^4$ and $B_{\delta} = 3Q_{\delta}/R^4$, and P_2 denotes the Legendre polynomial of order 2. From this, we see that the magnetic field of a general quadrupole is completely specified by the basis vectors $\{\hat{\mathbf{q}}_i\}$, and the field strengths B_{\parallel} and B_{δ} . Figure 1 illustrates the geometry of these field components.

The above composition of the surface quadrupole magnetic field completely specifies the external EM fields, which give rise to an inertial torque (see Appendix for calculation)

$$\begin{aligned} \Gamma_Q &= \frac{B_{\parallel}^2 R^5}{175 c^2} (\boldsymbol{\omega} \cdot \hat{\mathbf{q}}_1) (\boldsymbol{\omega} \times \hat{\mathbf{q}}_1) \\ &+ \frac{4B_{\parallel} B_{\delta} R^5}{525 c^2} [(\boldsymbol{\omega} \cdot \hat{\mathbf{q}}_3) (\boldsymbol{\omega} \times \hat{\mathbf{q}}_3) - (\boldsymbol{\omega} \cdot \hat{\mathbf{q}}_1) (\boldsymbol{\omega} \times \hat{\mathbf{q}}_1)] \\ &- \frac{4B_{\delta}^2 R^5}{1575 c^2} [(\boldsymbol{\omega} \cdot \hat{\mathbf{q}}_3) (\boldsymbol{\omega} \times \hat{\mathbf{q}}_3) + (\boldsymbol{\omega} \cdot \hat{\mathbf{q}}_2) (\boldsymbol{\omega} \times \hat{\mathbf{q}}_2)]. \end{aligned} \quad (13)$$

The form of this torque differs from Good & Ng (1985). The torque calculated in Good & Ng (1985) is expressed in Cartesian coordinates, with $\hat{\boldsymbol{\omega}} = \hat{\mathbf{z}}$, while the expression

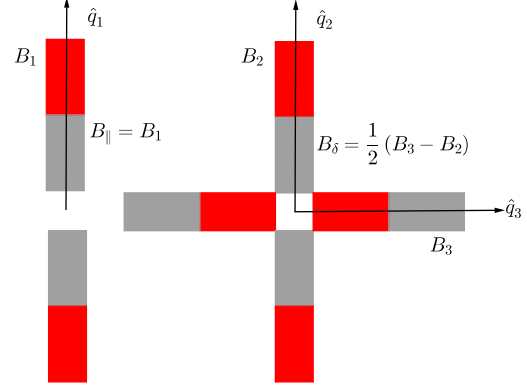


Figure 1. Two components of the quadrupole field. A general quadrupole field is specified by three principal axes ($\hat{\mathbf{q}}_1$, $\hat{\mathbf{q}}_2$, $\hat{\mathbf{q}}_3$), in which the quadrupole tensor is diagonal, and two elements (Q_{\parallel} and Q_{δ}) with the corresponding surface magnetic fields B_{\parallel} and B_{δ} .

above is basis independent. For convenience, we define two new dimensionless parameters:

$$\epsilon_{\parallel} \equiv \frac{1}{175} \frac{B_{\parallel}^2 R^5}{I c^2}, \quad (14)$$

$$\epsilon_{\delta} \equiv \frac{4}{1575} \frac{B_{\delta}^2 R^5}{I c^2}. \quad (15)$$

With these definitions, the inertial magnetic quadrupole torque takes the form

$$\begin{aligned} \Gamma_Q &= I \epsilon_{\parallel} (\boldsymbol{\omega} \cdot \hat{\mathbf{q}}_1) (\boldsymbol{\omega} \times \hat{\mathbf{q}}_1) \\ &+ 2I \sqrt{\epsilon_{\parallel} \epsilon_{\delta}} [(\boldsymbol{\omega} \cdot \hat{\mathbf{q}}_3) (\boldsymbol{\omega} \times \hat{\mathbf{q}}_3) - (\boldsymbol{\omega} \cdot \hat{\mathbf{q}}_1) (\boldsymbol{\omega} \times \hat{\mathbf{q}}_1)] \\ &- I \epsilon_{\delta} [(\boldsymbol{\omega} \cdot \hat{\mathbf{q}}_3) (\boldsymbol{\omega} \times \hat{\mathbf{q}}_3) + (\boldsymbol{\omega} \cdot \hat{\mathbf{q}}_2) (\boldsymbol{\omega} \times \hat{\mathbf{q}}_2)]. \end{aligned} \quad (16)$$

2.3 Magnetic Inertia Tensor

To re-express the torques given by equations (8) and (16), we define two tensors \mathbf{M}_P and \mathbf{M}_Q , associated with the inertia of the dipole and quadrupole magnetic fields:

$$\mathbf{M}_P \equiv -I \epsilon_P (\hat{\mathbf{p}} \otimes \hat{\mathbf{p}}), \quad (17)$$

$$\begin{aligned} \mathbf{M}_Q &\equiv -I \epsilon_{\parallel} (\hat{\mathbf{q}}_1 \otimes \hat{\mathbf{q}}_1) \\ &- 2I \sqrt{\epsilon_{\parallel} \epsilon_{\delta}} (\hat{\mathbf{q}}_3 \otimes \hat{\mathbf{q}}_3 - \hat{\mathbf{q}}_1 \otimes \hat{\mathbf{q}}_1) \\ &+ I \epsilon_{\delta} (\hat{\mathbf{q}}_3 \otimes \hat{\mathbf{q}}_3 + \hat{\mathbf{q}}_2 \otimes \hat{\mathbf{q}}_2). \end{aligned} \quad (18)$$

The Magnetic Inertia Tensor \mathbf{M} is defined to be

$$\mathbf{M} \equiv \mathbf{M}_P + \mathbf{M}_Q, \quad (19)$$

so that the inertial torque takes the form

$$\Gamma_{\text{inert}} = \Gamma_P + \Gamma_Q = -\boldsymbol{\omega} \times (\mathbf{M} \cdot \boldsymbol{\omega}). \quad (20)$$

This new form of the inertial torque Γ_{inert} given by equation (20) will be used in the next section.

3 NON-DISSIPATIVE PRECESSION

In this section, we solve the equation of motion for the NS rotation analytically, incorporating a non-spherical rigid body moment of inertia tensor and the inertial torques from co-rotating dipole and quadrupole magnetic fields. We neglect the radiative torque, and derive an analytic expression for

precession period. Melatos (1999, 2000) has previously presented numerical solutions for such non-dissipative precession, incorporating only the dipole torque.

3.1 Explicit Solution for Non-Dissipative Precession

The Euler equation for the NS rotation takes the form

$$\mathbf{I} \cdot \frac{d\boldsymbol{\omega}}{dt} + \boldsymbol{\omega} \times (\mathbf{I} \cdot \boldsymbol{\omega}) = \boldsymbol{\Gamma}_{\text{inert}}, \quad (21)$$

where \mathbf{I} is the ‘‘intrinsic’’ moment of inertia tensor for the NS. The derivative d/dt is taken in the frame with the body. Substituting expression (20) into the dynamical equation (21) and re-arranging gives

$$\mathbf{I} \cdot \frac{d\boldsymbol{\omega}}{dt} + \boldsymbol{\omega} \times [(\mathbf{I} + \mathbf{M}) \cdot \boldsymbol{\omega}] = 0. \quad (22)$$

To solve this system analytically, we define an effective inertia tensor \mathbf{I}_{eff} as

$$\mathbf{I}_{\text{eff}} \equiv \mathbf{I} + \mathbf{M}. \quad (23)$$

As long as the magnitude $|\mathbf{M}|/I$ is much less than unity, or $\epsilon_P, \epsilon_{\parallel}, \epsilon_{\delta} \ll 1$, we can replace the first term in (22) by $\mathbf{I}_{\text{eff}} \cdot d\boldsymbol{\omega}/dt$. This approximation is valid in the full regime of interest [see Eq. (45), (46), and (47) below]. Equation (22) then becomes

$$\frac{d\mathbf{L}}{dt} + \boldsymbol{\omega} \times \mathbf{L} = 0, \quad (24)$$

where $\mathbf{L} \equiv \mathbf{I}_{\text{eff}} \cdot \boldsymbol{\omega}$ is the effective angular momentum of the body, including the inertia term from the near-zone magnetic field.

Equation (24) is the equation of motion for a freely precessing rigid body, and has a well known analytic solution which we will summarize. Because \mathbf{I}_{eff} is a real 3×3 symmetric tensor, it may be diagonalized. Let $\hat{\mathbf{e}}_{\text{eff},3}$, $\hat{\mathbf{e}}_{\text{eff},2}$, and $\hat{\mathbf{e}}_{\text{eff},1}$ denote the three eigenvectors (the principal axes) of \mathbf{I}_{eff} with the respective eigenvalues $I_{\text{eff},3} > I_{\text{eff},2} > I_{\text{eff},1}$. In this frame, equation (24) has the conserved quantities

$$\frac{L_1^2}{I_{\text{eff},1}} + \frac{L_2^2}{I_{\text{eff},2}} + \frac{L_3^2}{I_{\text{eff},3}} = 2E, \quad (25)$$

$$L_1^2 + L_2^2 + L_3^2 = L^2, \quad (26)$$

where E is the rotational energy of the body and L is the angular momentum. The evolution of the components of $\hat{\mathbf{L}} \equiv \mathbf{L}/L$ can be obtained by solving equation (24) (see Landau & Lifshitz 1969 Chapter 6; Akgün et al. 2006):

$$\begin{aligned} \hat{L}_1 &= -\Lambda \text{cn}(\phi, k^2), \\ \hat{L}_2 &= -\Lambda \sqrt{1 + e^2} \text{sn}(\phi, k^2), \\ \hat{L}_3 &= \sqrt{1 - \Lambda^2} \text{dn}(\phi, k^2), \end{aligned} \quad (27)$$

when $L^2 > 2EI_{\text{eff},2}$ and

$$\begin{aligned} \hat{L}_1 &= -\Lambda \text{dn}(k\phi, k^{-2}), \\ \hat{L}_2 &= -\sqrt{(1 - \Lambda^2)(1 + e^{-2})} \text{sn}(k\phi, k^{-2}), \\ \hat{L}_3 &= \sqrt{1 - \Lambda^2} \text{cn}(k\phi, k^{-2}), \end{aligned} \quad (28)$$

when $L^2 < 2EI_{\text{eff},2}$. Here cn, sn, and dn are the Jacobian

Elliptic functions, and

$$\Lambda = \sqrt{\frac{I_{\text{eff},1}(2EI_{\text{eff},3} - L^2)}{L^2(I_{\text{eff},3} - I_{\text{eff},1})}}, \quad (29)$$

$$\phi = t\omega_p, \quad (30)$$

$$\omega_p = \frac{\epsilon_{\text{eff}} L \sqrt{1 - \Lambda^2}}{I_{\text{eff},3} \sqrt{1 + e^2}}, \quad (31)$$

$$k^2 = \frac{e^2 \Lambda^2}{1 - \Lambda^2}, \quad (32)$$

$$\epsilon_{\text{eff}} = \frac{I_{\text{eff},3} - I_{\text{eff},1}}{I_{\text{eff},1}}, \quad (33)$$

$$e^2 = \frac{I_{\text{eff},3}(I_{\text{eff},2} - I_{\text{eff},1})}{I_{\text{eff},1}(I_{\text{eff},3} - I_{\text{eff},2})}. \quad (34)$$

Equations (27) imply precession around $\hat{\mathbf{e}}_{\text{eff},3}$, and equations (28) imply precession around $\hat{\mathbf{e}}_{\text{eff},1}$. This shows the main effect of the inertial torque is to modify the equations of motion from that of a freely-precessing body with moment of inertia \mathbf{I} to a freely-precessing body with a modified moment of inertia \mathbf{I}_{eff} .

An effectively biaxial body corresponds to the special cases of $e = 0$ or $e = \infty$. When $e = 0$, equations (27) simplify to

$$\begin{aligned} \hat{L}_1 &= -\sin \theta \cos \phi, \\ \hat{L}_2 &= -\sin \theta \sin \phi, \\ \hat{L}_3 &= \cos \theta, \end{aligned} \quad (35)$$

where

$$\phi = \cos \theta \epsilon_{\text{eff}} \omega t \quad (36)$$

with $\Lambda = \sin \theta$ and $\cos \theta = \hat{\boldsymbol{\omega}} \cdot \hat{\mathbf{e}}_{\text{eff},3}$. When $e = \infty$, equations (28) simplify to

$$\begin{aligned} \hat{L}_1 &= -\cos \theta, \\ \hat{L}_2 &= -\sin \theta \sin(k\phi), \\ \hat{L}_3 &= \sin \theta \cos(k\phi). \end{aligned} \quad (37)$$

where

$$k\phi = \cos \theta \epsilon_{\text{eff}} \omega t \quad (38)$$

and $\Lambda = \cos \theta = \hat{\boldsymbol{\omega}} \cdot \hat{\mathbf{e}}_{\text{eff},1}$.

3.2 Numerical examples

In this subsection, we illuminate the solutions of equation (24) with some illustrative examples. We define a body axis $\{\hat{\mathbf{e}}_i\}$, corresponding to the eigenvectors of the axis-symmetric tensor \mathbf{I} , with an intrinsic ellipticity $\epsilon \equiv (I_3 - I_1)/I_3$ and a dimensionless angular velocity parameter $\hat{\boldsymbol{\omega}} \equiv \boldsymbol{\omega}/\omega$. Figures 2 and 3 show the time evolution of $\hat{\boldsymbol{\omega}}$. In both figures, an intrinsically biaxial star is assumed, with $\epsilon = 10^{-11}$ (see sec. 4.1) and the symmetry axis along $\hat{\mathbf{e}}_3$.

Figure 2 shows how the dynamics are modified by a dipole magnetic field with $\epsilon_P = 2.4 \times 10^{-12}$ and direction $\hat{\mathbf{p}}$ oriented in the (13) plane with angle $\chi = 10^\circ$. The fact that $\hat{\mathbf{e}}_{\text{eff},3} \cdot \hat{\boldsymbol{\omega}} \simeq \text{const.}$ indicates that $\hat{\boldsymbol{\omega}}$ is precessing around $\hat{\mathbf{e}}_{\text{eff},3}$, with slight variations due to the fact that \mathbf{I}_{eff} is slightly triaxial. Figure 3 adds a quadrupole magnetic field with $\epsilon_{\parallel} = \epsilon_P$, $\epsilon_{\delta} = 0$, and

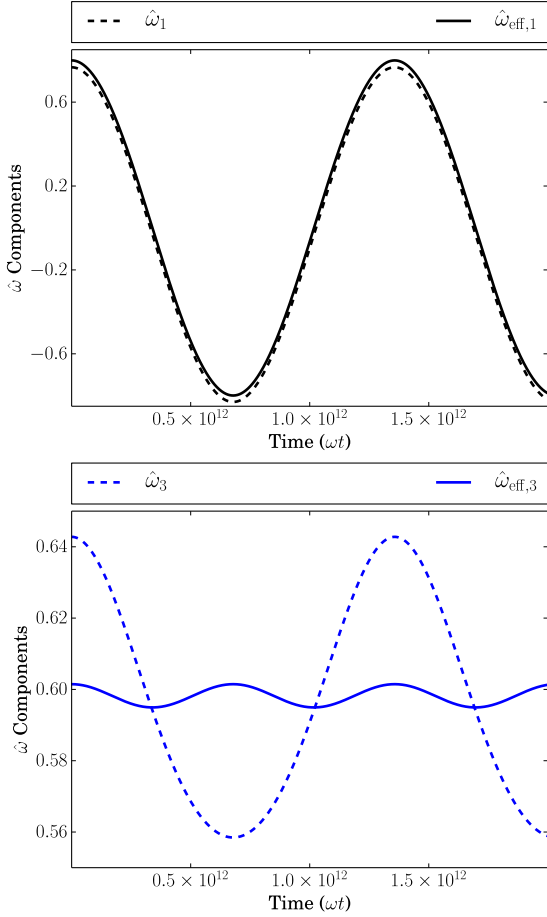


Figure 2. Components of the angular velocity unit vector $\hat{\omega} = \boldsymbol{\omega}/\omega$ obtained by integrating equation (22). The components are $\hat{\omega}_i = \hat{\mathbf{e}}_i \cdot \hat{\boldsymbol{\omega}}$ (dashed line) and $\hat{\omega}_{\text{eff},i} = \hat{\mathbf{e}}_{\text{eff},i} \cdot \hat{\boldsymbol{\omega}}$ (solid line). We assume a biaxial star with ellipticity $\epsilon = 10^{-11}$, and $\hat{\mathbf{p}}$ oriented in the (13)-plane with angle $\chi = 10^\circ$, and $\epsilon_P = 2.4 \times 10^{-12}$. We assume that $\epsilon_Q = 0$. In the $\{\hat{\mathbf{e}}_i\}$ basis, $\hat{\mathbf{e}}_1 = (1, 0, 0)$, $\hat{\mathbf{e}}_{\text{eff},1} = (0.9986, 0, 0.05277)$, $\hat{\mathbf{e}}_3 = (0, 0, 1)$ and $\hat{\mathbf{e}}_{\text{eff},3} = (-0.05277, 0, 0.9986)$. Note $\hat{\mathbf{e}}_2 = \hat{\mathbf{e}}_{\text{eff},2}$. The initial conditions are $\hat{\mathbf{e}}_1 \cdot \hat{\boldsymbol{\omega}} = \sin(50^\circ)$, $\hat{\mathbf{e}}_2 \cdot \hat{\boldsymbol{\omega}} = 0$, and $\hat{\mathbf{e}}_3 \cdot \hat{\boldsymbol{\omega}}(0) = \cos(50^\circ)$. The fact that $\hat{\mathbf{e}}_{\text{eff},3} \cdot \hat{\boldsymbol{\omega}} \simeq \text{const.}$ indicates that $\hat{\boldsymbol{\omega}}$ is precessing around $\hat{\mathbf{e}}_{\text{eff},3}$, and the small variation is due to the fact that \mathbf{I}_{eff} is slightly triaxial.

$\hat{\mathbf{q}}_1 = [\sin(60^\circ) \cos(205^\circ), \sin(60^\circ) \sin(205^\circ), \cos(60^\circ)]$. Notice that $\hat{\mathbf{e}}_{\text{eff},3} \cdot \hat{\boldsymbol{\omega}}$ is no longer constant, which follows from a more triaxial \mathbf{I}_{eff} than the example displayed in Figure (2).

The solutions to equation (24) are periodic in time, with periods T_1 and T_3 for precession around $\hat{\mathbf{e}}_{\text{eff},1}$ and $\hat{\mathbf{e}}_{\text{eff},3}$ respectively. The explicit relation for T_1 and T_2 are given by

$$T_1 = \frac{4I_{\text{eff},1}}{\epsilon_{\text{eff}}L} \sqrt{\frac{1+e^{-2}}{1-\Lambda^2}} \frac{K(k^{-2})}{k}, \quad (39)$$

$$T_3 = \frac{4I_{\text{eff},3}}{\epsilon_{\text{eff}}L} \sqrt{\frac{1+e^2}{1-\Lambda^2}} K(k^2), \quad (40)$$

where K is the complete elliptic integral of the first kind. The reason why we do not have the simple relation $T = 2\pi/\omega_p$ is because the Jacobi Elliptic functions are not 2π periodic, but rather $4K(k^2)$ periodic. For the special cases

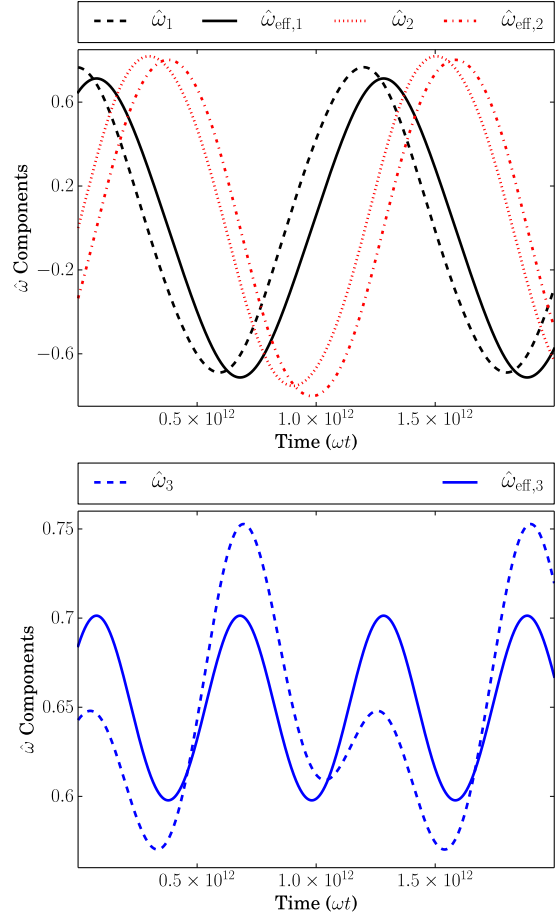


Figure 3. Same as Figure 2, except we have added a quadrupole inertial torque with $\epsilon_{\parallel} = \epsilon_P$, $\epsilon_{\delta} = 0$, and $\hat{\mathbf{q}}_1 = [\sin(60^\circ) \cos(205^\circ), \sin(60^\circ) \sin(205^\circ), \cos(60^\circ)]$ in the basis $\{\hat{\mathbf{e}}_i\}$. Because $\epsilon_{\delta} = 0$, $\hat{\mathbf{q}}_2$ and $\hat{\mathbf{q}}_3$ are irrelevant. Notice that $\hat{\mathbf{e}}_{\text{eff},3} \cdot \hat{\boldsymbol{\omega}}$ is no longer constant, because the tensor \mathbf{I}_{eff} is much more tri-axial.

$e = 0$ or $e = \infty$, these relations simplify to

$$T_1 = T_3 = \frac{2\pi}{\epsilon_{\text{eff}}\omega \cos \theta}. \quad (41)$$

One can show that the periods (39) and (40) give the periods displayed in Figures 2 and 3.

4 APPLICATION TO PULSARS

In the previous section, we showed that the effect of the inertial torque is to add an effective deformation in the moment of inertia of the NS. In this section we apply this formalism to pulsars. We begin with going over the relative magnitudes of NS deformations, then examine the behavior of the magnetic inclination angle over different timescales, and lastly discuss the possibility of explaining the magnetic counter-alignment of the Crab pulsar with precession.

4.1 Neutron Star Deformations

There are several physical causes for the moment of inertia tensor \mathbf{I} of a NS to depart from spherical symmetry. The first

is due to interior magnetic fields, which gives an intrinsic body ellipticity $\epsilon = (I_3 - I_1)/I_1$ of order

$$\begin{aligned}\epsilon_{\text{mag}} &= \beta \frac{R^4 B_*^2}{GM^2} \\ &= 2 \times 10^{-12} \beta \left(\frac{B_*}{10^{12} \text{ G}} \right)^2 \left(\frac{R}{10^6 \text{ cm}} \right)^4 \left(\frac{M}{1.4 M_\odot} \right)^{-2},\end{aligned}\quad (42)$$

where B_* is the internal magnetic field strength, and β is a dimensionless constant which depends on the geometry of the internal field. For a dipole or toroidal magnetic field topology, β is of order unity (Mastrano et al. 2013).

The second source is rotation. A uniform density fluid star rotating with angular velocity ω has an ellipticity of

$$\epsilon_{\text{fluid}} = \frac{15}{16\pi} \frac{\omega^2}{G\rho}, \quad (43)$$

where ρ is the density. The NS is likely to have deformations of this order early in its lifetime. Once the NS crust crystallizes, the body is able to support hydrostatic stresses. If we idealize the crust as having a uniform shear modulus μ , the part of the ellipticity which does not align with the rotation axis is (Munk & MacDonald 1975)

$$\begin{aligned}\epsilon_{\text{elastic}} &= \frac{\tilde{\mu}}{1 + \tilde{\mu}} \epsilon_{\text{fluid}} = 2 \times 10^{-11} \left(\frac{\mu}{10^{30} \text{ dynes/cm}^2} \right) \\ &\times \left(\frac{P}{1 \text{ sec.}} \right)^{-2} \left(\frac{R}{10^6 \text{ cm}} \right)^7 \left(\frac{M}{1.4 M_\odot} \right)^{-3},\end{aligned}\quad (44)$$

where $\tilde{\mu} = 19\mu/(2\rho gR)$, g is the surface gravity, and μ is the fiducial value for the shear modulus for the crust, evaluated at the density of order $\sim 10^{14} \text{ g/cm}^3$. This is a simple order of magnitude estimate of $\epsilon_{\text{elastic}}$. More detailed calculations for realistic NS parameters may be found in Cutler et al. (2003).

We compare these ‘‘intrinsic’’ deformations in the moment of inertial \mathbf{I} to the effective moments of inertia induced by co-rotating magnetic fields. These are

$$\epsilon_P = 1.5 \times 10^{-13} \left(\frac{B_P}{10^{12} \text{ G}} \right)^2 \left(\frac{R}{10^6 \text{ cm}} \right)^5 \left(\frac{M}{1.4 M_\odot} \right)^{-1}, \quad (45)$$

$$\epsilon_{\parallel} = 5.7 \times 10^{-15} \left(\frac{B_{\parallel}}{10^{12} \text{ G}} \right)^2 \left(\frac{R}{10^6 \text{ cm}} \right)^5 \left(\frac{M}{1.4 M_\odot} \right)^{-1}, \quad (46)$$

$$\epsilon_{\delta} = 2.5 \times 10^{-15} \left(\frac{B_{\delta}}{10^{12} \text{ G}} \right)^2 \left(\frac{R}{10^6 \text{ cm}} \right)^5 \left(\frac{M}{1.4 M_\odot} \right)^{-1}. \quad (47)$$

Thus, the biggest correction to the moment of inertia tensor \mathbf{I}_{eff} comes from ϵ_P , assuming that the quadrupole and dipole field strengths are similar. In order for the corrections due to the quadrupole field to dominate over that of the dipole, one needs either $B_{\parallel} \gtrsim 5B_P$ or $B_{\delta} \gtrsim 7B_P$.

We note that ϵ_P is always at least an order of magnitude smaller than ϵ_{mag} (since $B_* \gtrsim B$), and is smaller than $\epsilon_{\text{elastic}}$ for realistic NS parameters. Of course, ϵ_P may be directly inferred from the measured P and \dot{P} of the pulsar:

$$\epsilon_P \approx \frac{9}{40\pi^2} \frac{c}{R} P \dot{P}. \quad (48)$$

This gives an observational lower bound on the effective ellipticity ϵ_{eff} associated with \mathbf{I}_{eff} [see Eq. (23)]:

$$|\epsilon_{\text{eff}}| \sim |\epsilon_P + \epsilon_{\text{elastic}} + \epsilon_{\text{mag}} + \epsilon_{\parallel} + \epsilon_{\delta}| \gtrsim |\epsilon_P|. \quad (49)$$

4.2 Evolution of magnetic inclination angle: analytic result for biaxial bodies

Before presenting general results and applications in section 4.3, we first summarize the key analytic results of Goldreich (1970) for an effectively biaxial body ($e = 0, \infty$). We define three angles χ , θ , and α by

$$\cos \chi = \hat{\mathbf{p}} \cdot \hat{\mathbf{e}}_{\text{eff},3}, \quad \cos \theta = \hat{\boldsymbol{\omega}} \cdot \hat{\mathbf{e}}_{\text{eff},3}, \quad \cos \alpha = \hat{\boldsymbol{\omega}} \cdot \hat{\mathbf{p}}. \quad (50)$$

We assume that the magnetic field axis $\hat{\mathbf{p}}$ is frozen into the body, so that the angle χ is constant in time. The other two angles in general will evolve.

On timescales much shorter than the pulsar spindown time, the variation of α is due to precession:

$$\frac{d\alpha}{dt} \approx \omega_p \sin \chi \csc \alpha \sin \theta \sin(\omega_p t), \quad (51)$$

where $\omega_p = \cos \theta \epsilon_{\text{eff}} \omega$.

Over timescales comparable to the pulsar the spindown time, the precession can be averaged out, giving (Goldreich 1970):

$$\frac{1}{\omega} \left\langle \frac{d\omega}{dt} \right\rangle \simeq -\frac{2p^2 \omega^2}{3c^3 I} \left[\sin^2 \chi + \sin^2 \theta \left(1 - \frac{3}{2} \sin^2 \chi \right) \right], \quad (52)$$

$$\frac{1}{\sin \theta} \left\langle \frac{d \sin \theta}{dt} \right\rangle \simeq -\frac{2p^2 \omega^2}{3c^3 I} \cos^2 \theta \left(1 - \frac{3}{2} \sin^2 \chi \right). \quad (53)$$

From relation (53), we see that θ always evolves toward 0° or 90° , depending on if the angle χ is greater or less than the critical angle $\chi_{\text{crit}} = \sin^{-1}(\sqrt{2/3}) \simeq 55^\circ$. This evolution takes place over the radiative timescale

$$\begin{aligned}\tau_{\text{rad}} &= \frac{3c^3 I}{2p^2 \omega^2} = 7 \times 10^7 \\ &\times \left(\frac{M}{1.4 M_\odot} \right) \left(\frac{P}{1 \text{ s}} \right)^2 \left(\frac{R}{10^6 \text{ cm}} \right)^{-4} \left(\frac{B_P}{10^{12} \text{ G}} \right)^{-2} \text{ years.}\end{aligned}\quad (54)$$

The magnetic inclination angle α is related to θ and $\phi = \omega_p t$ (the precession phase), and χ , through the relation

$$\cos \alpha = \hat{\boldsymbol{\omega}} \cdot \hat{\mathbf{p}} = \cos \chi \cos \theta + \sin \chi \sin \theta \cos \phi. \quad (55)$$

Using equation (53) and averaging over ϕ , we obtain

$$\left\langle \frac{d \sin^2 \alpha}{dt} \right\rangle \simeq -\frac{p^2 \omega^2}{3c^3 I} \sin^2(2\theta) \left(1 - \frac{3}{2} \sin^2 \chi \right)^2. \quad (56)$$

This shows that α always decreases over timescales much longer than the precession period, but not necessarily to zero. From equation (55), we see if $\theta \rightarrow 0$, then α evolves to χ , and if $\theta \rightarrow \pi/2$, then α evolves to $\pi/2 - \chi$.

4.3 Counter-alignment of the Crab Pulsar

The Crab pulsar has $P = 0.0331 \text{ s}$ and $\dot{P} = 4.22 \times 10^{-13} \text{ s/s}$, implying the characteristic age of $P/2\dot{P} = 1240 \text{ years}$, and dipole field of order $B_P \sim 4 \times 10^{12} \text{ G}$. Through modeling the Crab pulsar pulse profile, many authors have estimated

α to be in the range of $45^\circ - 70^\circ$ (Harding et al. 2008; Watters et al. 2009; Du et al. 2012). The minimum effective ellipticity of the NS arises from the inertia of the dipole field, $\epsilon_P \sim 2.4 \times 10^{-12}$. This would give a minimum precession frequency $\omega_p \gtrsim \epsilon_p \omega \sim 0.8^\circ/\text{year}$. The observed $d\alpha/dt$ is $0.6^\circ/\text{century}$ (Lyne et al. 2013). Since $\omega_p \gg d\alpha/dt$, to explain the observed $d\alpha/dt$ with precession [see Eq. (51)], we require either $\chi \ll 1$ (the effective principal axis $\hat{\mathbf{e}}_{\text{eff},3}$ is almost aligned with the dipole axis) or $\theta \ll 1$ ($\hat{\mathbf{e}}_{\text{eff},3}$ is almost aligned with the rotation axis). This would correspond to one of two special cases: the NS is dominated by stresses from the dipole magnetic field, or from rotation/elasticity.

Figures 4 and 5 depict two examples of the evolution of the magnetic inclination angle for a NS with an effectively biaxial \mathbf{I}_{eff} and $\epsilon_{\text{eff}} = 4 \times 10^{-11}$. This value could result from the elastic part of the rotational distortion [see (44)] or from the magnetic distortion associated with an internal field B_* larger than the dipole field [see (42)]. Figure 4 shows the case with $\chi = 0.15^\circ$, so that the principal axis $\hat{\mathbf{e}}_{\text{eff},3}$ is nearly aligned with $\hat{\mathbf{p}}$, while Figure 5 corresponds to the case with an initial $\theta = 0.1^\circ$, so that $\hat{\mathbf{e}}_{\text{eff},3}$ is nearly aligned with $\hat{\boldsymbol{\omega}}$. In both cases, α increases during half of the precession phase, with $\dot{\alpha}$ consistent with the value $0.6^\circ/100$ years observed by Lyne et al. (2013).

Figure 6 depicts an example similar to Fig. 4 except with $\epsilon_{\text{eff}} = 4 \times 10^{-11}$ and $\chi = 1.0^\circ$. This value of ϵ_{eff} is close to the lower limit set by ϵ_P (associated with the inertia of the dipole field). Note that with a mixture of comparable inertial poloidal and toroidal fields, the magnetic distortion ϵ_{mag} [Eq. (42)] can be reduced (Mastrano et al. 2013). The rotational distortion $\epsilon_{\text{elastic}}$ [Eq. (44)] would not affect the precession if aligned with the spin axis. Both sets of parameters (Fig. 4 and 6) can account for the observed $d\alpha/dt$ of the Crab pulsar. In the case of Figure 6, the $\dot{\alpha} > 0$ lasts for ~ 200 years because of the long precession period ($2\pi/\omega_p \propto \epsilon_{\text{eff}}^{-1}$), whereas in the case of Figure 4, the $\dot{\alpha} > 0$ phase lasts ~ 20 years.

In both Figures 4 and 6, we see a secular decrease of α over many precession cycles, with $\langle \dot{\alpha} \rangle \sim -1^\circ/100$ years. Figure 5 does not display a large secular change in α . This is because equations (52) and (53) predict θ stays close to zero, so $\alpha \sim \text{constant}$ according to equation (56).

4.4 First and second order braking indexes

Also plotted on Figure 6 is the braking index $n = (\omega\ddot{\omega})/\dot{\omega}^2$, computed using equation (1). We see that during the time when $\dot{\alpha} \sim 1^\circ/100$ years, the currently observed value of $n = 2.5$ is reproduced. However, during the time when $\dot{\alpha} < 0$, a much larger value of n is expected. Thus continued observations of n in the coming decades will test whether precession is responsible for the currently observed $\dot{\alpha}$ for the Crab pulsar.

Modeling the dynamical evolution of the Crab pulsar through precession also gives predictions of the second order braking index, defined through $m \equiv (\ddot{\omega} \omega^2)/\dot{\omega}^3$. By rewriting in terms of n and \dot{n} (Melatos 1997), we have

$$m = n(2n - 1) + \frac{\omega}{\dot{\omega}} \dot{n}, \quad (57)$$

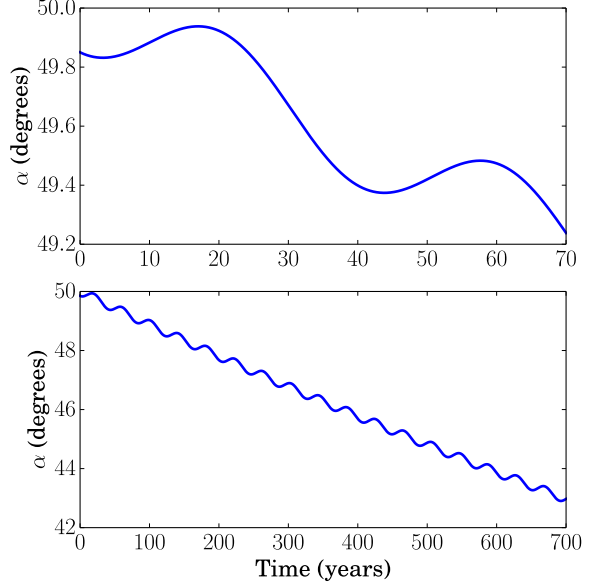


Figure 4. Evolution of magnetic inclination angle of a NS with an effectively biaxial \mathbf{I}_{eff} , with $\epsilon_{\text{eff}} = 4 \times 10^{-11}$. The initial conditions are $\hat{\mathbf{e}}_{\text{eff},1} \cdot \hat{\boldsymbol{\omega}} = \sin(50^\circ)$, $\hat{\mathbf{e}}_{\text{eff},2} \cdot \hat{\boldsymbol{\omega}} = 0$, and $\hat{\mathbf{e}}_{\text{eff},3} \cdot \hat{\boldsymbol{\omega}} = \cos(50^\circ)$. The upper panel shows the variation over decade timescales. We assume $\chi = 0.15^\circ$, which here is the angle between the dipole axis and the principal body axis $\hat{\mathbf{e}}_{\text{eff},3}$.

and using equations (1) and (51),

$$m = n(2n - 1) + (3 - n)(n - 1) - 2(\dot{\alpha})^2 \left(\frac{\omega}{\dot{\omega}}\right)^2 (\cot^2 \alpha + \csc^2 \alpha) + 2 \left(\frac{\omega}{\dot{\omega}}\right)^2 \dot{\alpha} \omega_P \cot(\omega_P t). \quad (58)$$

With the observed $\dot{\alpha} = 0.6^\circ/\text{century}$ and $\omega/\dot{\omega} = -24.9$ century, and the estimate $\alpha \approx 45^\circ$ (Harding et al. 2008), we find

$$m \approx 10.1 + 3.5 \left(\frac{\cos \theta}{1}\right) \left(\frac{\epsilon_{\text{eff}}}{10^{-11}}\right) \cot(\omega_P t). \quad (59)$$

If $\cot(\omega_P t) \approx 0$, we find precession gives an excellent agreement with the inferred 1993 value of $m \simeq 10.1$ for the Crab pulsar (Lyne et al. 1993). An evolving precession phase ($\omega_P t$) may in part explain the increase of the second order braking index to $m \simeq 45.6$ (Lyne et al. 2015).

We caution that our model does not include magnetospheric effects on the electromagnetic torque. For example, if we adapt the spindown law (Spitkovsky 2006)

$$\dot{\omega} \propto -\omega^3 (1 + \sin^2 \alpha), \quad (60)$$

then equation (1) should be changed to

$$n = 3 + 2 \frac{\omega \sin \alpha \cos \alpha}{\dot{\omega} (1 + \sin^2 \alpha)} \dot{\alpha}. \quad (61)$$

Thus, to account for $n \simeq 2.50$ would require $\dot{\alpha} \approx 1.7^\circ/100$ years, assuming $\alpha \approx 45^\circ$. The evolution of n would be modified, along with the value of m .

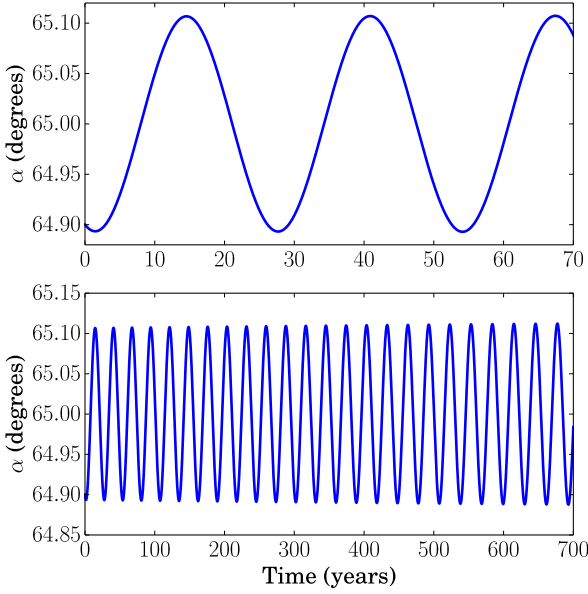


Figure 5. Same as Figure 4, except with $\chi = 65^\circ$ and an initial $\theta = 0.1^\circ$, which is the angle between the rotation axis and the principal body axis $\hat{\mathbf{e}}_{\text{eff},3}$. In other words, the initial conditions are $\hat{\mathbf{e}}_{\text{eff},1} \cdot \hat{\boldsymbol{\omega}}(0) = \sin(0.1^\circ) \sin(65^\circ)$, $\hat{\mathbf{e}}_{\text{eff},2} \cdot \hat{\boldsymbol{\omega}}(0) = 0$, and $\hat{\mathbf{e}}_{\text{eff},3} \cdot \hat{\boldsymbol{\omega}}(0) = \cos(0.1^\circ) \cos(65^\circ)$.

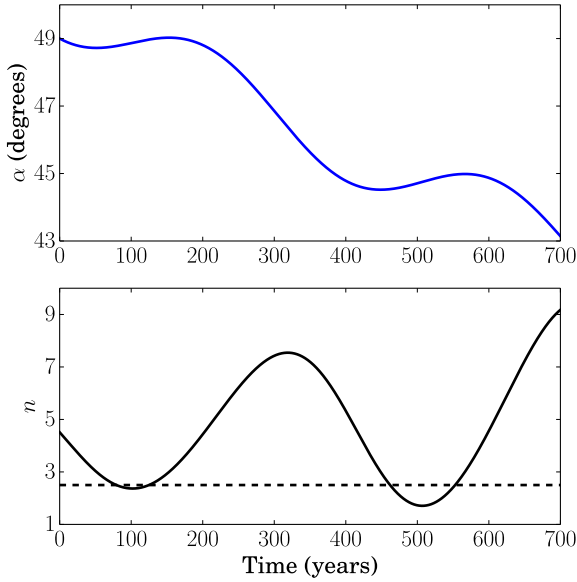


Figure 6. The evolution of magnetic inclination angle α (upper panel) and the braking index n (lower panel). The parameters are the same as Fig. 4, except with $\epsilon_{\text{eff}} = 4 \times 10^{-12}$ and $\chi = 1.0^\circ$. The currently observed value $n = 2.5$ is indicated by the dashed line.

5 DISCUSSION AND CONCLUSION

In this paper, we have studied the rotational dynamics of magnetic neutron stars (NSs), modeled as a non-spherical rigid body acted upon by electromagnetic (EM) torques. First, we presented new calculations of the near-field EM torques associated with the magnetic inertia of the dipole

and quadrupole fields of a NS in vacuum [Eqs. (3) and (13)]. Our analytical results show that if the NS has a quadrupole field a few times stronger than the dipole field, the inertial quadrupole torque can become more important than the corresponding dipole torque. Second, we showed that, despite the complexity of the inertial torque expressions, the effects of these torques amount to a modification to the intrinsic moment of inertia tensor of the star [see Eqs. (17)-(19) and (23)]. In general, the effective moment of inertia tensor is triaxial even for an intrinsically biaxial NS. This allows us to understand analytically the key effects of the inertial torques on the precessional dynamics of magnetic NSs. Finally, we applied our theoretical results to the Crab pulsar in order to understand the physical origin of the recently observed counter-alignment of the pulsar’s magnetic inclination angle α (Lyne et al. 2013, 2015). We showed that it is possible to explain the increase of α on decade timescales through precession. However, since the typical precession frequency ω_p is much greater than the observed rate $d\alpha/dt$, this explanation requires some fine-tuning of the principal axes $\{\hat{\mathbf{e}}_{\text{eff},i}\}$ of the effective moment of inertia tensor \mathbf{I}_{eff} : $\hat{\mathbf{e}}_{\text{eff},3}$ must be almost aligned with the magnetic dipole axis or the spin axis. This apparent fine-tuning may be expected if the star’s intrinsic distortion arises primarily from the dipole field or from the rotation. Over timescales comparable to the pulsar’s age, the magnetic inclination α always decreases (see Figs. 4-6).

If the observed counter-alignment of magnetic inclination of the Crab pulsar is indeed caused by precession, then the sign of $d\alpha/dt$ will switch to negative after half a precession period. Future observations would provide useful test and constrain the precession frequency (and thus the distortion of the pulsar). Note that the upper bound on the time which the pulsar should take to reverse its counter-alignment behavior is $t \lesssim \epsilon_P^{-1} P/2 \sim 200$ years [see Eq. (45)]. Thus it is not unreasonable to suspect that the behavior of α may switch from counter-alignment to alignment within a human lifetime.

There are several complications and uncertainties neglected in our model and calculations:

(i) Our treatment of the crustal elasticity gave only an order of magnitude estimate of $\epsilon_{\text{elastic}}$, ignoring complications such as the NS equation of state and the thickness of the crust.

(ii) The internal magnetic field structure was mostly ignored, restricting our evaluation of ϵ_{mag} to an order of magnitude estimate.

(iii) We assumed that the only dissipative process was the radiative spindown torque. Other dissipative processes such as polar wandering (Macy 1974) and crust-core couplings (Shaham 1977; Alpar et al. 1984; Alpar & Oegelman 1987; Casini & Montemayor 1998; Sedrakian et al. 1999; Link & Cutler 2002) may significantly affect the NS rotation/precession dynamics.

(iv) The exterior of the NS was assumed to be a vacuum, which is well known to not be true. The presence of a magnetosphere may change the inertial torques acting on the NS.

Any one of these effects may affect the dynamical evolution of α , and further work is necessary to determine if their inclusions will change the main results of this paper.

ACKNOWLEDGMENTS

We thank Andrew Melatos, Michael Kramer, Ira Wasserman, and James Cordes for useful discussions, and the anonymous reviewer for quick and thoughtful suggestions improving the quality of our paper. This work has been supported in part by NSF grant AST-1211061, and NASA grants NNX12AF85G, NNX14AG94G and NNX14AP31G.

REFERENCES

Akgin, T., Link, B., & Wasserman, I. 2006, MNRAS, 365, 653
 Alpar, M. A., Anderson, P. W., Pines, D., & Shaham, J. 1984, ApJ, 278, 791
 Alpar, M. A., Pines, D., Anderson, P. W., & Shaham, J. 1984, ApJ, 276, 325
 Alpar, A., & Oegelman, H. 1987, A&A, 185, 196
 Beskin, V. S., & Zheltoukhov, A. A. 2014, Physics Uspekhi, 57, 799
 Beskin, V. S., Zheltoukhov, A. A., Obukhova, A. K., & Stroinov, E. E. 2013, Bulletin of the Lebedev Physics Institute, 40, 265
 Casini, H., & Montemayor, R. 1998, ApJ, 503, 374
 Ciolfi, R., Ferrari, V., Gualtieri, L., & Pons, J. A. 2009, MNRAS, 397, 913
 Cutler, C., Ushomirsky, G., & Link, B. 2003, ApJ, 588, 975
 Deutsch, A. J. 1955, Annales d’Astrophysique, 18, 1
 Davis, L., & Goldstein, M. 1970, ApJL, 159, L81
 Du, Y. J., Qiao, G. J., & Wang, W. 2012, ApJ, 748, 84
 Faucher-Giguère, C.-A., & Kaspi, V. M. 2006, ApJ, 643, 332
 Glampedakis, K., & Jones, D. I. 2010, MNRAS, 405, L6
 Goldreich, P. 1970, ApJL, 160, L11
 Goldreich, P., & Julian, W. H. 1969, ApJ, 157, 869
 Good, M. L., & Ng, K. K. 1985, ApJ, 299, 706
 Gullón, M., Miralles, J. A., Viganò, D., & Pons, J. A. 2014, MNRAS, 443, 1891
 Harding, A. K., & Lai, D. 2006, Reports on Progress in Physics, 69, 2631
 Harding, A. K., Stern, J. V., Dyks, J., & Frackowiak, M. 2008, ApJ, 680, 1378
 Jackson, J. D. 1998, Classical Electrodynamics, 3rd Edition, by John David Jackson, pp. 832. ISBN 0-471-30932-X. Wiley-VCH, July 1998.,
 Jones, D. I. 2012, MNRAS, 420, 2325
 Jones, D. I., & Andersson, N. 2001, MNRAS, 324, 811
 Kalapotharakos, C., & Contopoulos, I. 2009, A&A, 496, 495
 Kalapotharakos, C., Kazanas, D., Harding, A., & Contopoulos, I. 2012, ApJ, 749, 2
 Kaspi, V. M. 2010, Proceedings of the National Academy of Science, 107, 7147
 Landau, L. D., & Lifshitz, E. M. 1960, Electrodynamics of continuous media,
 Landau, L. D., & Lifshitz, E. M. 1969, Course of Theoretical Physics, Oxford: Pergamon Press, 1969, 2nd ed.,
 Link, B., & Cutler, C. 2002, MNRAS, 336, 211
 Link, B., & Epstein, R. I. 1997, ApJL, 478, L91
 Link, B., & Epstein, R. I. 2001, ApJ, 556, 392
 Lyne, A. G., Pritchard, R. S., & Smith, F. G. 1988, MNRAS, 233, 667

Lyne, A. G., Pritchard, R. S., & Graham-Smith, F. 1993, MNRAS, 265, 1003
 Lyne, A., Graham-Smith, F., Weltevrede, P., et al. 2013, Science, 342, 598
 Lyne, A. G., Jordan, C. A., Graham-Smith, F., et al. 2015, MNRAS, 446, 857
 Macy, W. W., Jr. 1974, ApJ, 190, 153
 Makishima, K., Enoto, T., Hiraga, J. S., et al. 2014, Physical Review Letters, 112, 171102
 Mastrano, A., Lasky, P. D., & Melatos, A. 2013, MNRAS, 434, 1658
 Melatos, A. 1997, MNRAS, 288, 1049
 Melatos, A. 1999, ApJL, 519, L77
 Melatos, A. 2000, MNRAS, 313, 217
 Munk, W. H., & MacDonald, G. J. F. 1975, The rotation of the earth: a geophysical discussion., by Munk, W. H.; MacDonald, G. J. F.. First published 1960. Cambridge (UK): Cambridge University Press, 19 + 323 p.,
 Philippov, A., Tchekhovskoy, A., & Li, J. G. 2014, MNRAS, 441, 1879
 Reisenegger, A. 2013, arXiv:1305.2542
 Rookyard, S. C., Weltevrede, P., & Johnston, S. 2015, MNRAS, 446, 3356
 Sedrakian, A., Wasserman, I., & Cordes, J. M. 1999, ApJ, 524, 341
 Shaham, J. 1977, ApJ, 214, 251
 Spitkovsky, A. 2006, ApJL, 648, L51
 Stairs, I. H., Lyne, A. G., & Shemar, S. L. 2000, Nature, 406, 484
 Suto, Y., & Iso, K.-I. 1985, Ap&SS, 115, 243
 Tauris, T. M., & Manchester, R. N. 1998, MNRAS, 298, 625
 Tchekhovskoy, A., Spitkovsky, A., & Li, J. G. 2013, MNRAS, 435, L1
 Truemper, J., Kahabka, P., Oegelman, H., Pietsch, W., & Voges, W. 1986, ApJL, 300, L63
 Wasserman, I. 2003, MNRAS, 341, 1020
 Watters, K. P., Romani, R. W., Weltevrede, P., & Johnston, S. 2009, ApJ, 695, 1289
 Weisberg, J. M., Everett, J. E., Cordes, J. M., Morgan, J. J., & Brisbin, D. G. 2010, ApJ, 721, 1044
 Weltevrede, P., & Johnston, S. 2008, MNRAS, 387, 1755
 Young, M. D. T., Chan, L. S., Burman, R. R., & Blair, D. G. 2010, MNRAS, 402, 1317

6 APPENDIX: EM TORQUES ON A ROTATING MAGNETIC SPHERE IN VACUUM

We begin with the magnetic field in the co-rotating frame of the star “frozen in” to the body. In the inertial frame, the magnetic field rigidly co-rotates with the star, maintaining the same shape and magnitudes as in the rotating frame. If the star is perfectly conducting, the electric field inside the star in the inertial frame is given *exactly* by $\mathbf{E} = -(\mathbf{v}/c) \times \mathbf{B}$ (Landau & Lifshitz 1960). If we work in the spherical coordinates (r, θ, ϕ) , the coordinate transformation from the co-rotating frame to the inertial frame is $\phi \rightarrow \phi - \omega t$, where ω is the rotation rate. If the surface of the star is given by $r = R$, the electromagnetic fields must satisfy the boundary conditions $(\mathbf{r} \cdot \mathbf{B})_{r=R^+} = (\mathbf{r} \cdot \mathbf{B})_{r=R^-}$ and

$(\mathbf{r} \times \mathbf{E})_{r=R-} = (\mathbf{r} \times \mathbf{E})_{R=R+}$. Thus, the external EM fields of the rotating star are uniquely determined by the normal components of the magnetic field at the stellar surface.

The complete solution of the EM fields in vacuum in terms of multipole moments is derived in Jackson (1998). These fields, separated into time-independent terms \mathbf{B}_0 and \mathbf{E}_0 , and time-dependent terms \mathbf{E}' and \mathbf{B}' , may be re-expressed in terms of vector spherical harmonics:

$$\mathbf{B}_0 = \sum_{\ell} \left[(\ell+1)a_M(\ell, 0) \left(\frac{x_0}{x}\right)^{\ell+2} \mathbf{Y}_{\ell 0} - a_M(\ell, 0) \left(\frac{x_0}{x}\right)^{\ell+2} \Psi_{\ell 0} \right], \quad (62)$$

$$\mathbf{E}_0 = \sum_{\ell} \left[(\ell+1)a_E(\ell, 0) \left(\frac{x_0}{x}\right)^{\ell+2} \mathbf{Y}_{\ell 0} - a_E(\ell, 0) \left(\frac{x_0}{x}\right)^{\ell+2} \Psi_{\ell 0} \right], \quad (63)$$

$$\mathbf{B}' = \sum_{\ell, m \neq 0} \left\{ -i \frac{a_E(\ell, m)}{\sqrt{\ell(\ell+1)}} h_{\ell}(mx) \Phi_{\ell m} + \sqrt{\ell(\ell+1)} a_M(\ell, m) \frac{h_{\ell}(mx)}{mx} \mathbf{Y}_{\ell m} + \frac{a_M(\ell, m)}{\sqrt{\ell(\ell+1)}} \left[\frac{h_{\ell}(mx) + mx h'_{\ell}(mx)}{mx} \right] \Psi_{\ell m} \right\}, \quad (64)$$

$$\mathbf{E}' = \sum_{\ell, m \neq 0} \left\{ -\sqrt{\ell(\ell+1)} a_E(\ell, m) \frac{h_{\ell}(mx)}{mx} \mathbf{Y}_{\ell m} - \frac{a_E(\ell, m)}{\sqrt{\ell(\ell+1)}} \left[\frac{h_{\ell}(mx) + mx h'_{\ell}(mx)}{mx} \right] \Psi_{\ell m} - i \frac{a_M(\ell, m)}{\sqrt{\ell(\ell+1)}} h_{\ell}(mx) \Phi_{\ell m} \right\}, \quad (65)$$

where

$$\begin{aligned} \mathbf{Y}_{\ell m} &\equiv Y_{\ell m}(\theta, \phi - \omega t) \hat{\mathbf{r}}, \\ \Psi_{\ell m} &\equiv r \nabla Y_{\ell m}(\theta, \phi - \omega t), \\ \Phi_{\ell m} &\equiv \mathbf{r} \times \nabla Y_{\ell m}(\theta, \phi - \omega t), \end{aligned} \quad (66)$$

with $x \equiv r\omega/c$ and $Y_{\ell m}$ denote spherical harmonics. The actual fields are given by the real parts of \mathbf{E} and \mathbf{B} . Defining $q_{\ell m} \equiv \int d\Omega (\mathbf{B} \cdot \hat{\mathbf{r}})_{r=R}$, the boundary conditions give the multi-pole moments:

$$\begin{aligned} a_M(\ell, m) &= \begin{cases} \frac{q_{\ell 0}}{\ell+1} & m=0 \\ \frac{q_{\ell m}}{\sqrt{\ell(\ell+1)}} \frac{mx_0}{h_{\ell}(mx_0)} & m \neq 0 \end{cases} \quad (67) \\ a_E(\ell, m) &= \begin{cases} \frac{x_0}{\ell(\ell+1)} \left[(1 - \delta_{\ell 0}) \ell J_{(\ell+1)0} q_{(\ell+1)0} - (\ell+1) J_{\ell 0} q_{(\ell-1)0} \right] & m=0 \\ \frac{x_0}{\sqrt{\ell(\ell+1)}} \frac{mx_0}{h_{\ell}(mx_0) + mx_0 h'_{\ell}(mx_0)} \times \left[\ell J_{(\ell+1)m} q_{(\ell+1)m} - (\ell+1) J_{\ell m} q_{(\ell-1)m} \right] & m \neq 0 \end{cases} \quad (68) \end{aligned}$$

where $x_0 \equiv R\omega/c$, $\delta_{\ell m}$ is the Kronecker delta, and

$$J_{\ell m} \equiv \begin{cases} \sqrt{\frac{\ell^2 - m^2}{4\ell^2 - 1}} & \text{if } |m| < \ell \\ 0 & \text{if } |m| \geq \ell \end{cases} \quad (69)$$

The Kronecker delta term forces charge neutrality.

It may be shown that for $\ell = 1$ the above expressions reproduce the solution by Deutsch (1955) [see Melatos (1997)

for corrections]. For this work, we are interested in both the $\ell = 1$ and $\ell = 2$ terms. Let the unit vector in the direction of the dipole moment be $\hat{\mathbf{p}}$, and the three unit eigenvectors for the quadrupole moment be $\hat{\mathbf{q}}_1$, $\hat{\mathbf{q}}_2$, and $\hat{\mathbf{q}}_3$ (see Fig 1). If the magnetic field consists only of $\ell = 1$ term, we may define the magnitude of B_P as $B_P = B(R, \hat{\mathbf{p}})$, where the notation $B(r, \hat{\mathbf{n}})$ denotes the magnetic field evaluated at r with angular coordinates in the direction of the unit vector $\hat{\mathbf{n}}$. The quadrupole magnetic field has two independent components, due to the fact that the quadrupole tensor \mathbf{Q} is trace free (see Fig. 1). We define these to be $B_{\parallel} \equiv B(R, \hat{\mathbf{q}}_1)$ and $B_{\delta} \equiv [B(R, \hat{\mathbf{q}}_3) - B(R, \hat{\mathbf{q}}_2)]/2$.

The time-averaged EM Maxwell stress tensor is given by

$$\mathbf{T} = \frac{1}{4\pi} \text{Re} \left[\mathbf{E} \otimes \mathbf{E}^* + \mathbf{B} \otimes \mathbf{B}^* - \frac{1}{2} \delta (|E|^2 + |B|^2) \right], \quad (70)$$

where δ is the unit dyadic, and the stars denote the complex conjugate. One may decompose \mathbf{T} into spherical coordinates to evaluate the torque Γ in Cartesian coordinates:

$$\begin{aligned} \Gamma_x &= -R \int d\Omega [T_{r\theta} \sin \phi + T_{r\phi} \cos \theta \cos \phi]_{r=R}, \\ \Gamma_y &= R \int d\Omega [T_{r\theta} \cos \phi - T_{r\phi} \cos \theta \sin \phi]_{r=R}, \\ \Gamma_z &= R \int d\Omega [T_{r\phi} \sin \theta]_{r=R}, \end{aligned} \quad (71)$$

where $x + iy = r \sin \theta e^{i\phi}$, $z = r \cos \theta$.

After integrating equation (71), we expand the expressions in x_0 and only keep terms proportional to x_0^2 . We then arrive at equations (3) and (13).